Thermally reduced graphene/MXene film for enhanced Li-ion storage

Shuaikai Xu,[a] Yohan Dall'Agnese,[a] Junzhi Li,[a] Yury Gogotsi,*[a, b] and Wei Han*[a, c]

Abstract: Two-dimensional transition metal carbides called MXenes are emerging electrode materials for energy storage due to their metallic electrical conductivity and low ion diffusion barrier. In this work, we combined Ti_2CT_x MXene with graphene oxide (GO) followed by a thermal treatment to fabricate flexible rGO/Ti_2CT_r film, where electrochemically active rGO and Ti_2CT_r nanosheets impede the stacking of layers and synergistically interact producing ionically and electronically conducting electrodes. The effect of the thermal treatment on the electrochemical performance of Ti_2CT_x is evaluated. As anode for Li-ion storage, the thermally treated Ti_2CT_r possesses a higher capacity in comparison to as-prepared Ti_2CT_x. The freestanding hybrid rGO/Ti_2CT_r films exhibit excellent reversible capacity (700 mAh g^{-1} at 0.1 A g^{-1}), cycling stability and rate performance. Additionally, flexible rGO/$Ti_3C_2T_r$ films are made using the same method and also present improved capacity. Therefore, this study provides a simple, yet effective, approach to combine rGO with different MXenes, which can enhance their electrochemical properties for Li-ion batteries.

Introduction

Development of high-performance electrochemical energy storage devices has attracted increasing attention with the growing use of renewable energy sources,[1-3] and penetration of wearable devices into daily life. The Li-ion battery (LIB) is regarded as the most suitable candidate to satisfy energy storage needs due to its advanced development stage.[4-5] Many research efforts aim to develop advanced materials with higher capacities and lifetimes than current graphite or lithium titanate anodes.[6]

[a] Dr. S. Xu, Dr. Y. Dall'Agnese, Dr. J. Li, Prof. Y. Gogotsi, Prof. W. Han
Key Laboratory of Physics and Technology for Advanced Batteries (Ministry of Education)
Jilin University, Changchun 130012, (P.R. China)
E-mail: whan@jlu.edu.cn
[b] Prof. Y. Gogotsi
Department of Materials Science and Engineering, and A. J. Drexel Nanomaterials Institute
Drexel University, Philadelphia, Pennsylvania 19104, USA
E-mail: gogotsi@drexel.edu
[c] Prof. W. Han
International Center of Future Science
Jilin University, Changchun 130012, (P.R. China)

Two-dimensional (2D) materials such as graphene,[7] sulfides,[8,9] nitrides,[10,11] and oxides[12,13] have attracted considerable interest because of their unique and beneficial physical and chemical properties when used as LIB anode materials. However, limited electronic conductivity is an issue for many 2D materials. The largest family of highly conductive 2D materials is transition metal carbide/carbonitride labeled MXenes, which were discovered recently.[14] MXene are synthesized by selectively etching the A (Al, and other) layers from $M_{n+1}AX_n$ phases (where M is an early transition metal, X is carbon or nitrogen and n=1-3). When the A-layers are etched out, they are replaced by a combination of surface terminations such as OH, O and F, therefore the correct chemical designation for MXenes is $M_{n+1}X_nT_x$ (T_x refers to surface functional groups). MXenes are emerging as a promising anode material for Li-ion batteries [15] due to their metallic conductivity and 2D structure. Although $Ti_3C_2T_x$ and Ti_2CT_x have good electrical conductivity [16] and a low Li^+ diffusion barrier,[17] their capacity as anodes is not high enough compared to Sn, Si or other advanced nanomaterials. As-synthetized $Ti_3C_2T_x$ and Ti_2CT_x have capacities around 100 mAh/g at 1C rate,[18-20] which limits their application as electrode materials. To improve the capacity of $Ti_3C_2T_x$ anode, $Ti_3C_2T_x$ 'paper' was fabricated by filtering delaminated few-layer $Ti_3C_2T_x$ colloidal solution,[20] or producing hybrid $Ti_3C_2T_x$/carbon nanotubes electrodes.[21,22] More recently, Sn(+IV)-complexed ions decorating and pillaring highly conductive $Ti_3C_2T_x$ electrodes were used to produce anodes for advanced LIBs with outstanding capacities.[17,23] Additionally, it is predicted by DFT calculation that M_2C (M = Sc, Ti, V, and Cr) MXenes have gravimetric capacities over 400 mA h g^{-1}, which is higher than the gravimetric capacity of graphite, and can be doubled by forming Li metal bilayers between MXene layers.[24] Besides, the capacities of MXenes were predicted to significantly depend on the nature of surface terminal groups (-F, -O or -OH).[24-26] As the thinnest and lightest MXene, Ti_2CT_x, which is the closest to $Ti_3C_2T_x$ in composition, has a higher theoretical capacity than $Ti_3C_2T_x$ but lower conductivity.

Directly after synthesis, the electronic contact between the Ti_2CT_x MXene blocks is poor due to the large size of the particles, resulting in isolated MXene blocks and limiting the electrochemical performance. This problem can be solved by introducing conductive "bridges" to connect Ti_2CT_x particles.

Graphene, another important 2D material, has been widely used as an electrode for energy storage due to its good electronic conductivity, large theoretical specific surface area (~2630 $m^2 g^{-1}$), and superior mechanical properties.[26,27] It has been hybridized with $Ti_3C_2T_x$ MXene for supercapacitor applications.[28] Hence, by combining graphene with Ti_2CT_x it may be possible to improve the electrochemical performance of MXene-based anodes for Li-ion storage.[29,30]

In this work, flexible freestanding reduced graphene oxide (rGO)/Ti_2CT_r films were fabricated by vacuum-assisted filtration followed by thermal reduction under vacuum. During the thermal vacuum annealing, the surface terminal groups of Ti_2CT_x and graphene oxide (GO) were removed at the same time, resulting in improved electrical conductivity and bridging between Ti_2CT_r and rGO nanosheets. In addition, the Ti_2CT_x particles acted as conductive spacers and impeded the agglomeration of rGO nanosheets. The rGO/Ti_2CT_r films present enhanced electrochemical performance with high reversible capacity (~700 mAh g^{-1} at 0.1 A g^{-1}), high coulombic efficiency, excellent cycling stability and rate performance. To demonstrate that this approach proposed for rGO/Ti_2CT_r film anode can be applied to other MXenes, rGO/$Ti_3C_2T_r$ films were also fabricated by the same method and showed an improved electrochemical performance for Li-ion storage.

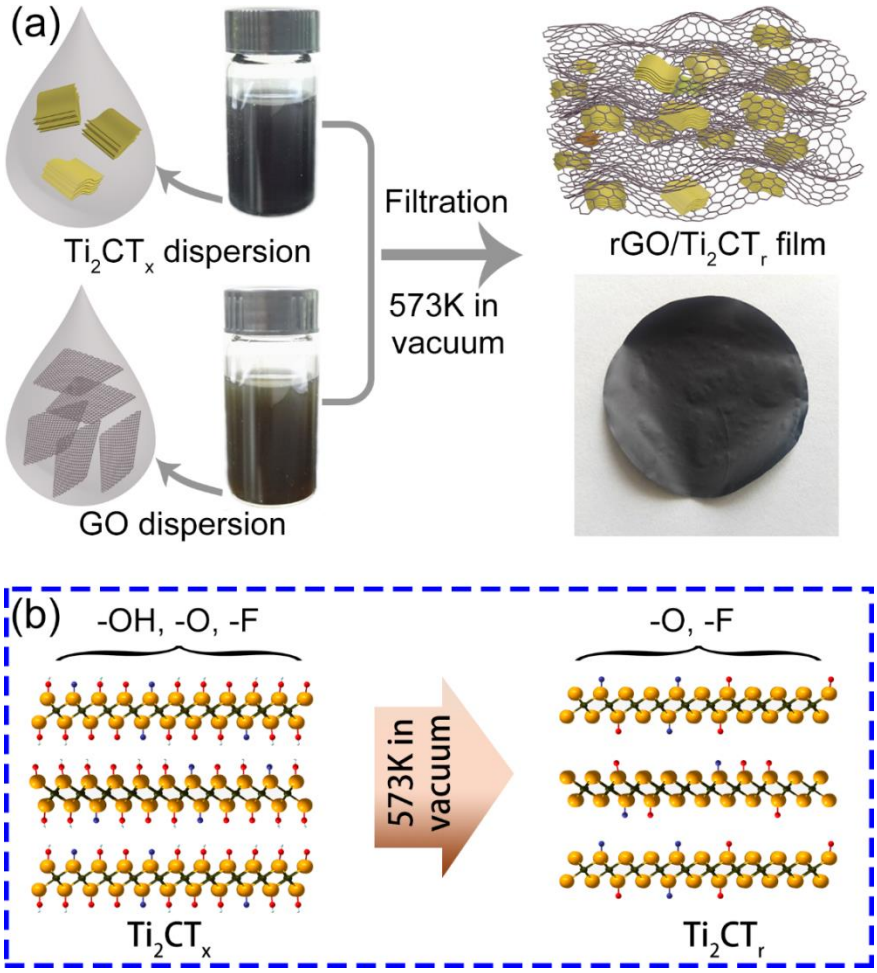

Figure 1. a) Schematic illustration of the fabrication process of the flexible rGO/Ti_2CT_r film and the digital photograph of the flexible rGO/Ti_2CT_r film. b) Schematic illustration of the surface modification process of Ti_2CT_x.

Results and Discussion

The flexible freestanding rGO/Ti_2CT_r films were produced following the process shown in Figure 1a. The rGO/Ti_2CT_r films were fabricated by vacuum-assisted filtration followed by thermal reduction at 573K for 5h under vacuum. During the thermal treatment process, the interlayer water and -OH terminal groups on the surface of Ti_2CT_x MXene were concomitantly removed (Figure 1b). To achieve the best flexibility and mechanical properties of rGO/Ti_2CT_r films, the weight ratio of rGO:Ti_2CT_r was

optimized and found to be 3:1 (details not shown in this work). Therefore, rGO/Ti_2CT_r films with the weight ratio of 3:1 were fabricated and characterized hereafter.

As shown in Figure 2a, after etching of Al from Ti_2AlC for 24h, the obtained Ti_2CT_x has a 2D layered structure, where the Ti_2CT_x layers were stacked into lamellas, indicating the successful etching. As shown in Figure S1a, after thermal reduction under vacuum, the Ti_2CT_r maintained 2D layered structure. The few-layer GO nanosheets present flat flake-like morphology (Figure S1b), but after thermal reduction under a vacuum, rGO nanosheets present a wrinkled morphology as shown in Figure 2b, which is caused by the removal of oxygen-containing functional group (-OH) from its surface. The rGO nanosheets possess a large lateral size and are a few layers thick. As a characteristic feature of rGO nanosheets, the presence of wrinkles and folds benefit the Li-ion transfer into rGO film. To further enhance the accessibility of the Li-ion to the film electrode and improve its electrochemical performance, Ti_2CT_x powders were introduced as conductive spacers between the rGO nanoflakes to produce flexible rGO/Ti_2CT_r films, whose typical cross-sectional FESEM images are shown in Figure 2d, e. rGO/Ti_2CT_r films possess more open structure than pure rGO (Figure S1c) or GO/Ti_2CT_x (Figure 2c) films due to the impeded stacking of rGO nanosheets by the embedded Ti_2CT_r particles and the thermal reduction process under vacuum. Figure S1d shows the top view FESEM image of the rGO/Ti_2CT_r films. Both the wrinkles and folds of the graphene and the embedded Ti_2CT_r particles were clearly observed. The results of the corresponding elemental mapping of Ti and C in Figure S1e, f indicated that the Ti_2CT_r particles were uniformly distributed into the hybrid rGO/Ti_2CT_r films. From Figure 2f, it can be observed that Ti_2CT_r particles are surrounded by wrinkled rGO nanosheets, improving the conductivity between distant Ti_2CT_r blocks. The measured BET specific surface areas of the GO/Ti_2CT_x and rGO/Ti_2CT_r films were 127 and 270 m^2 g^{-1}, respectively (Figure S1g). The increase of the BET-specific surface area is mainly attributed to the pore opening due to the gases released from rGO during reduction under vacuum. The pore width distributions of rGO/Ti_2CT_r films were evaluated by the BJH method, and the pore size was determined to be around 3 μm (Figure S1h and pores seen in Fig. 2e), which ensured a high ion-accessible surface area and low ion transport resistance.

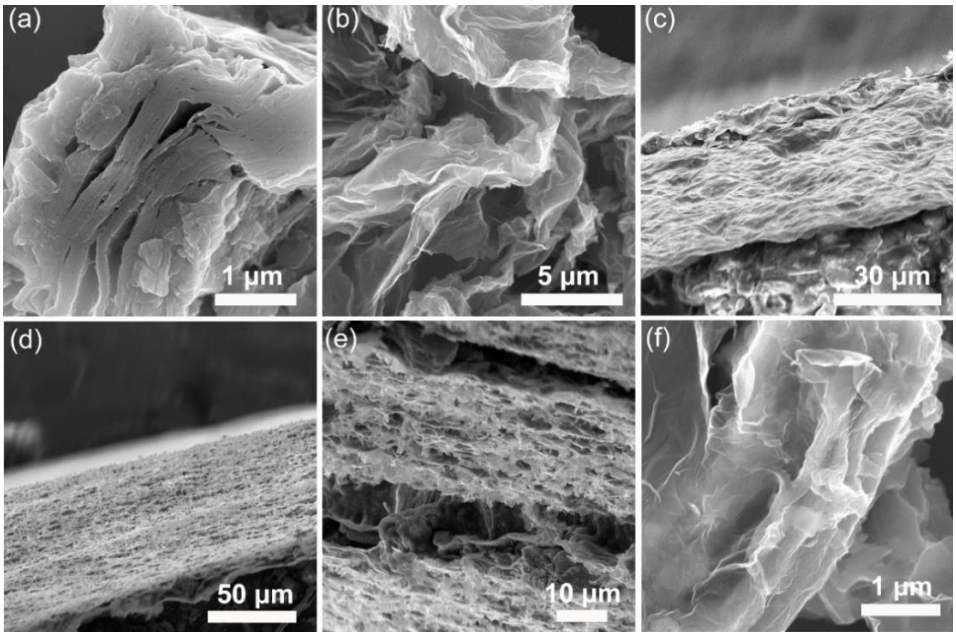

Figure 2. FESEM images of a) Ti_2CT_x and b) rGO nanosheets. c) FESEM cross section image of a hybrid GO/Ti_2CT_x film. d) Low- and e) high-magnification FESEM cross section images of a hybrid rGO/Ti_2CT_r film. f) High magnification FESEM image of Ti_2CT_r particles coated with rGO nanosheets.

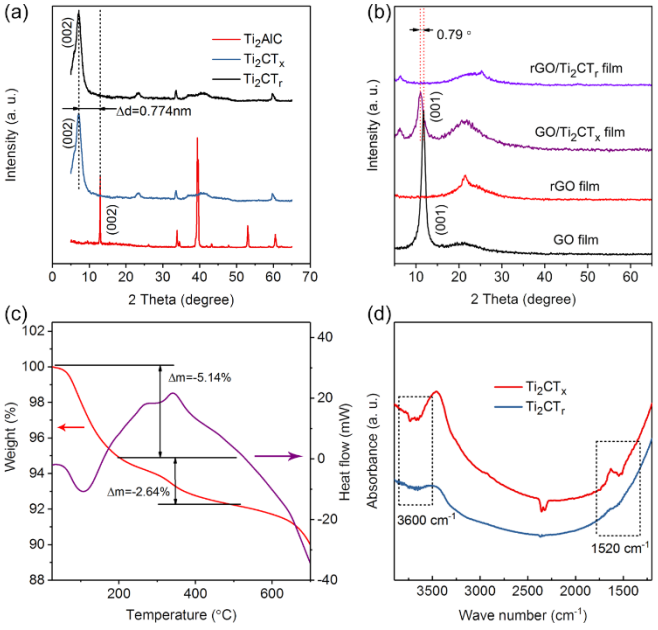

Figure 3. a) XRD patterns of Ti_2AlC before and after etching using HCl+LiF solution, and Ti_2CT_r. b) XRD patterns of pure GO, rGO film, hybrid GO/Ti_2CT_x, and rGO/Ti_2CT_r film. c) TG and DSC curves of Ti_2CT_x from room temperature to 700 ˚C in argon atmosphere. d) FT-IR spectra of Ti_2CT_x before and after thermal treatment.

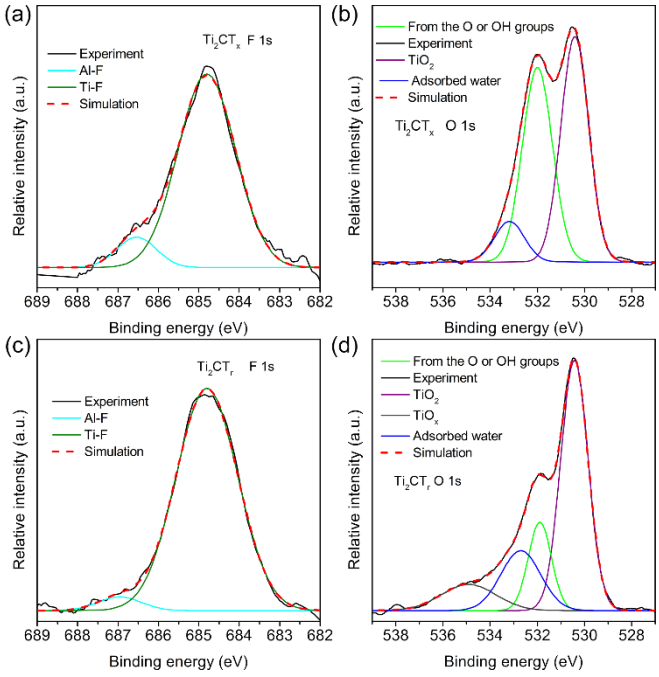

Figure 4. High-resolution XPS spectra of Ti_2CT_x and Ti_2CT_r in the F 1s (a, c) and O 1s (b, d) regions.

The phase composition of the materials was characterized by X-ray powder diffraction. When comparing the XRD patterns of the Ti_2AlC powders before and after HCl+LiF-etching (Figure 3a), it is clear that the (002) peak, which was initially at ≈13.0˚ 2θ, broadened and shifted to a lower angle of ≈7.1˚ 2θ after etching treatment, indicating that it shifted to a larger d spacing (Δd=0.774 nm). The peak of Ti_2AlC at ≈39.2˚ 2θ disappeared, suggesting the complete etching of Al from Ti_2AlC. Furthermore, the interlayer d spacing of HCl+LiF-etched Ti_2CT_x is much larger than that of the HF-etched Ti_2CT_x.[16,31] The large shifts are suggestive of the presence of water, and possibly cations (Li^+, H^+), between the hydrophilic and negatively charged Ti_2CT_x layers, similarly than reported observation on $Ti_3C_2T_x$.[32] Improved accessibility of interlayer spacing in HCl+LiF-etched Ti_2CT_x is expected to the intercalation of Li ions, improving the electrochemical capacity of the anode. The almost unchanged XRD profile of Ti_2CT_r compared with Ti_2CT_x showed that the MXene phase didn't change during the thermal treatment process. As shown in Figure 3b, for pure GO film, a broad diffraction peak at ≈10.1° 2θ is the typical peak corresponding to the layer-to-layer distance (d-spacing) of about 0.83 nm. However, after thermal reduction, the peak at ≈10.1˚ 2θ disappears, indicating a reduction of GO to form rGO film. The peak (001) at ≈10.1˚ 2θ of GO/Ti_2CT_x significantly shifted to the lower position and the half-peak width increased after introduction of Ti_2CT_x between GO nanosheets. This can be attributed to the fact that the embedded Ti_2CT_x prevent the ordering of stacked GO nanosheet. A similar phenomenon was also observed for rGO/Ti_2CT_r film comparing with rGO film, where the half-peak width also increased, demonstrating the successful combination of rGO nanosheets and Ti_2CT_r particles.

The surface structure is crucial for the electrochemical performance of MXene and thus several characterization techniques were applied. Thermogravimetric-differential scanning calorimetry (TG-DSC) analysis of HCl+LiF-etched Ti_2CT_x particles was carried out from room temperature to 700˚C in argon atmosphere (Figure 3c). The surface of as-prepared Ti_2CT_x is known to be terminated with F and/or OH. At high temperature, the -OH groups are lost or replaced by -O. It can be seen that the mass of Ti_2CT_x decreased with increased temperature. A weight loss of 5.14 % in the TG curve occurred from room temperature to about 200˚C, which is due to the loss of physically adsorbed water and residual acid on Ti_2CT_x surface.[33] The second stage weight loss of 2.64 % from 200˚C to 515˚C is caused by the loss of -OH groups attached on Ti_2CT_x surface.[34] Based on the results of TG-DSC analysis, the surface -OH groups in Ti_2CT_x can be eliminated by thermal reduction, similar to $Ti_3C_2T_x$.[26] To further confirm the release of -OH terminal groups by calcination at 300˚C, the Fourier transform infrared (FT-IR) measurement was also carried out for Ti_2CT_x before and after thermal treatment at 300˚C

under vacuum (Figure 3d). The peaks of the FT-IR spectra of Ti_2CT_x before thermal treatment at ~3600 and ~1520 cm^{-1} confirm the existence of -OH or strongly coordinated H_2O between Ti_2CT_x layers. After thermal reduction, these peaks weakened or disappeared, suggesting that the terminal -OH could be efficiently removed by calcination at 300˚C under vacuum. Oxygen terminal groups are preferred in Li-ion batteries. [24] XPS was used to characterize the chemical state of the Ti_2CT_x and Ti_2CT_r (Figure S2). The XPS spectra of Ti_2CT_x confirmed that the Al was removed and the surface was terminated by oxygen-containing functional groups (-OH, -O and -F). As shown in Figure 4a and c, the Ti_2CT_x and Ti_2CT_r samples all contain a large amount of -F terminated Ti. The intensity of the Ti-F peaks almost unchanged after thermal treatment, indicating the amount of -F surface group remains unchanged. It was noticed that traces of AlF_3 salt were present after Ti_2AlC phase etching. For Ti_2CT_x, a high-resolution spectrum in the O1s region (Figure 4b) could be fit by peaks at 530.5, 531.9 and 533.0 eV. The component centered at 530.5 eV is consistent with oxygen in TiO_2. The component centered at 531.9 eV likely arises from O or OH groups bound to the surface of the MXene layers. The peak centered at 533.0 eV can be attributed to strongly adsorbed water. These peaks are also observed in the high-resolution spectrum of Ti_2CT_r in the O1s region (Figure 4d). The intensity of the peaks at 530.5 and 532.9 eV was almost unchanged in comparison with that of Ti_2CT_x. However, the peak at 531.9 eV obviously decreases, which can be attributed to the removal of -OH surface group. Additionally, a peak at 535.0 eV appears, which likely arises from the formation TiO_x. The high-resolution XPS spectra in the F and O regions demonstrated that the -OH surface groups were effectively removed after thermal treatment, and MXene layers with mixed oxygen/fluorine terminations were formed.[35] This finding is consistent with the results of TG-DSC and FT-IR analyses.

The electrochemical performance of the rGO/Ti_2CT_r film was evaluated by tests in Li-ion half-cells, in which the rGO/Ti_2CT_r films served as the working electrodes and Li metal foils acted as both counter and reference electrodes. Firstly, the effect of the thermal treatment on the electrochemical performance of Ti_2CT_x is evaluated. As shown in Figure S3a and b, broad reversible peaks were observed for both Ti_2CT_x and Ti_2CT_r at 1.68 V vs. Li^+/Li during lithiation and delithiation in cycles from 2nd to 6th. Because the chemically adsorbed water or -OH terminations on surface of Ti_2CT_x were removed, these peaks can be tentatively assigned to the following redox intercalation reaction (Equation 1):[18]

$$Ti_2CO_xF_y + zLi^+ + ye^- \leftrightarrow Li_zTi_2CO_xF_y \quad (1)$$

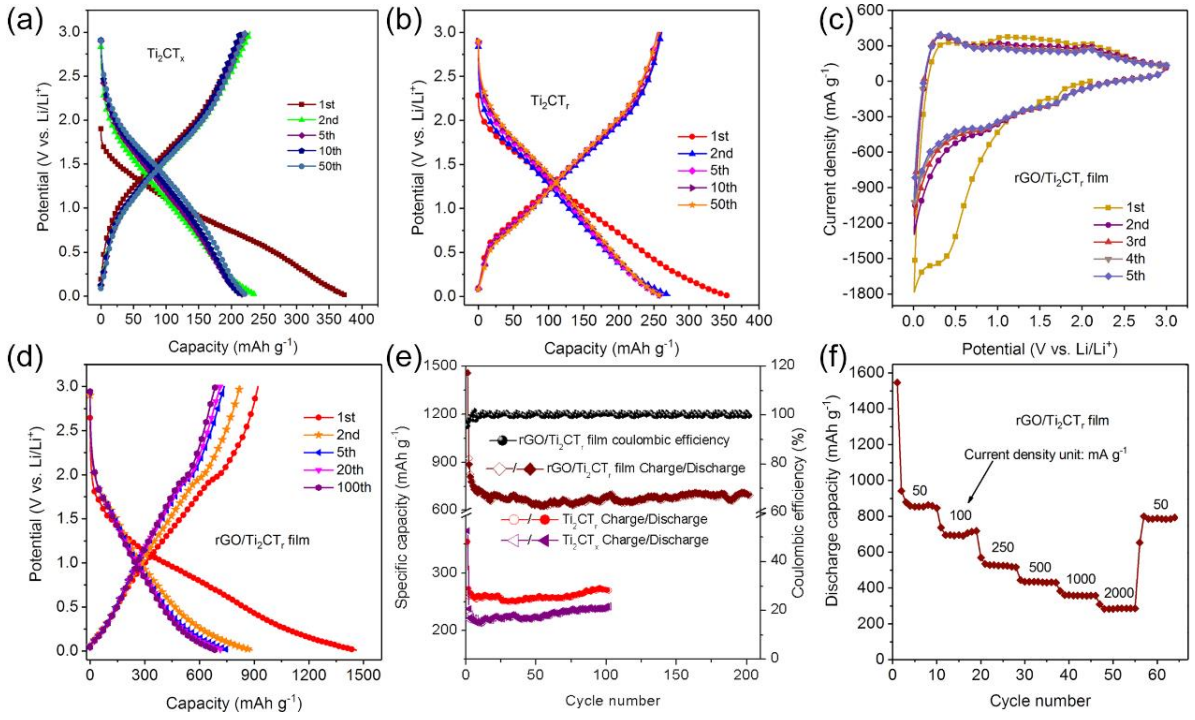

Figure 5. a) Charge/discharge profiles of Ti_2CT_x at current density of 0.1 A g^{-1}. b) Charge/discharge profiles of Ti_2CT_r at current density of 0.1 A g^{-1}. c) CV curves of rGO/Ti_2CT_r film at a scan rate of 0.5 mV s^{-1}. d) Charge-discharge profiles of rGO/Ti_2CT_r film at different cycles with a current density of 0.1 A g^{-1}. e) Cycling performance of Ti_2CT_x, Ti_2CT_r and rGO/Ti_2CT_r film at a current density of 0.1 A g^{-1}. f) Rate performance of hybrid rGO/Ti_2CT_r film electrode.

Figure 5a and b show the GCD curves of Ti_2CT_x and Ti_2CT_r at a current density of 0.1 A g^{-1}. The capacity loss in the first cycle can be attributed to the formation of solid electrolyte interphase (SEI) layer at potentials below 0.9 V vs. Li^+/Li. In the first cycle Ti_2CT_x shows higher capacity loss than Ti_2CT_r, which is attributed to the presence of –OH groups and intercalated water in Ti_2CT_x, leading to irreversible reaction during the first cycle. There is no obvious capacity loss after 100 cycles (Figure 5e) at current density of 0.1 A g^{-1}, revealing a good reversibility. As shown in Figure S3c, it can be observed that the redox peaks of Ti_2CT_r broadened compared to that of Ti_2CT_x, which is due to the removal of terminal -OH groups, increasing the number of active sites and possibly promoting the Li ions transport. As a result, Ti_2CT_r presented an improved capacity of 263 mAh g^{-1} (Figure S3d), which is higher than that of Ti_2CT_x (212 mAh g^{-1}). The improved electrochemical performance can be attributed to the enhanced electrical conductivity benefiting from the lower terminated surface group concentration after surface modification treatment.[24] Furthermore, in order to verify the good electrochemical performance of Ti_2CT_r in comparison with Ti_2CT_x, electrochemical impedance spectroscopy (EIS) was carried out using lithiated electrodes. Figure S4a compares the Nyquist plots of Ti_2CT_r and Ti_2CT_x. The typical characteristics of their Nyquist plots are a semicircle in the high- medium-frequency range and a sloping straight line in the low-frequency range. The diameter of the semicircle of Ti_2CT_r is much smaller than that of Ti_2CT_x, indicating that Ti_2CT_r possesses lower charge transfer resistance. The increased number of electrochemically active sites on Ti_2CT_r due to the removal of -OH terminations promoted the contact between the electrode material and electrolyte, causing a more effective charge-transfer process.

In the cyclic voltammetry (CV) profiles (Figure 5c) of rGO/Ti_2CT_r film, no obvious lithiation and delithiation peaks were observed, because of the introduction of rGO nanosheets [34]. The irreversible broad peak observed at 0.4 V vs. Li^+/Li during lithiation process in the first cycle is probably caused by the formation of SEI and possibly an irreversible reaction between Li ion and electrode materials (Ti_2CT_r or oxygen-containing functional groups on the rGO nanosheets). The charge/discharge profiles of the rGO/Ti_2CT_r film are presented in Figure 5d, which are measured between 0.01 and 3 V at a current density of 0.1 A g^{-1}. A long sloping voltage region over the range from 1.8 to 0.3 V can be attributed to the constant lithiation/delithiation process in rGO/Ti_2CT_r electrodes. In this work, gravimetric capacities are used to evaluate the performance of electrode materials. In the first cycle (Figure 5e), the discharge capacity of the rGO/Ti_2CT_r film electrode is 1460 mAh g^{-1}, while its charge capacity is 920 mAh g^{-1}, resulting in coulombic efficiency of 63%, which is higher than that of pure rGO film (42%, Figure S4b). The higher coulombic efficiency can be attributed to the impeded stacking of rGO nanosheets due to the introduction of Ti_2CT_r particles. The rGO/Ti_2CT_r film showed coulombic efficiencies near 100% and stable cycle performance after 5 cycles. At the 100th cycle, a reversible capacity of 700 mAh g^{-1} can still be retained, which is much larger than that of the graphene film electrode [36] and Ti_2CT_r (263 mAh g^{-1}) studied in this work.

The enhanced electrochemical performance of porous rGO/Ti_2CT_r film can be related to a few occurrences. During the thermal reduction process, the surface terminal groups of Ti_2CT_x and GO can be removed at the same time, resulting in good electronic contact between Ti_2CT_r and rGO nanosheets. There is no polymer binder additive needed as rGO acts as a conductive binder to tightly link the separated layers of Ti_2CT_r and connect the separated Ti_2CT_r particles, improving the conductivity of the anode. If there is a volume change of Ti_2CT_r during the charge/discharge process, the suitable mechanical properties of rGO would allow to retain the electric contact. In addition, the Ti_2CT_r particles could impede the agglomeration of rGO nanoflakes. From Figure S4a, it can be observed that rGO/Ti_2CT_r has a lower charge-transfer resistance in comparison with pure rGO film, which is also attributed to the higher electrical conductivity and porous hierarchical structure of the rGO/Ti_2CT_r electrode. The discharge/charge capacity of rGO/Ti_2CT_r film was observed at different current density, as shown in Figure 5f. The rGO/Ti_2CT_r film electrodes exhibited good specific capacities even at high rates. The corresponding discharge capacities at 50, 100, 250, 500, 1000, and 2000 mA g^{-1} are 853, 700, 558, 482, 401, and 325 mAh g^{-1}, respectively. It's important to stress that the elimination of binder and current collector that becomes possible with our electrodes, further improve the development process of Li-ion batteries.

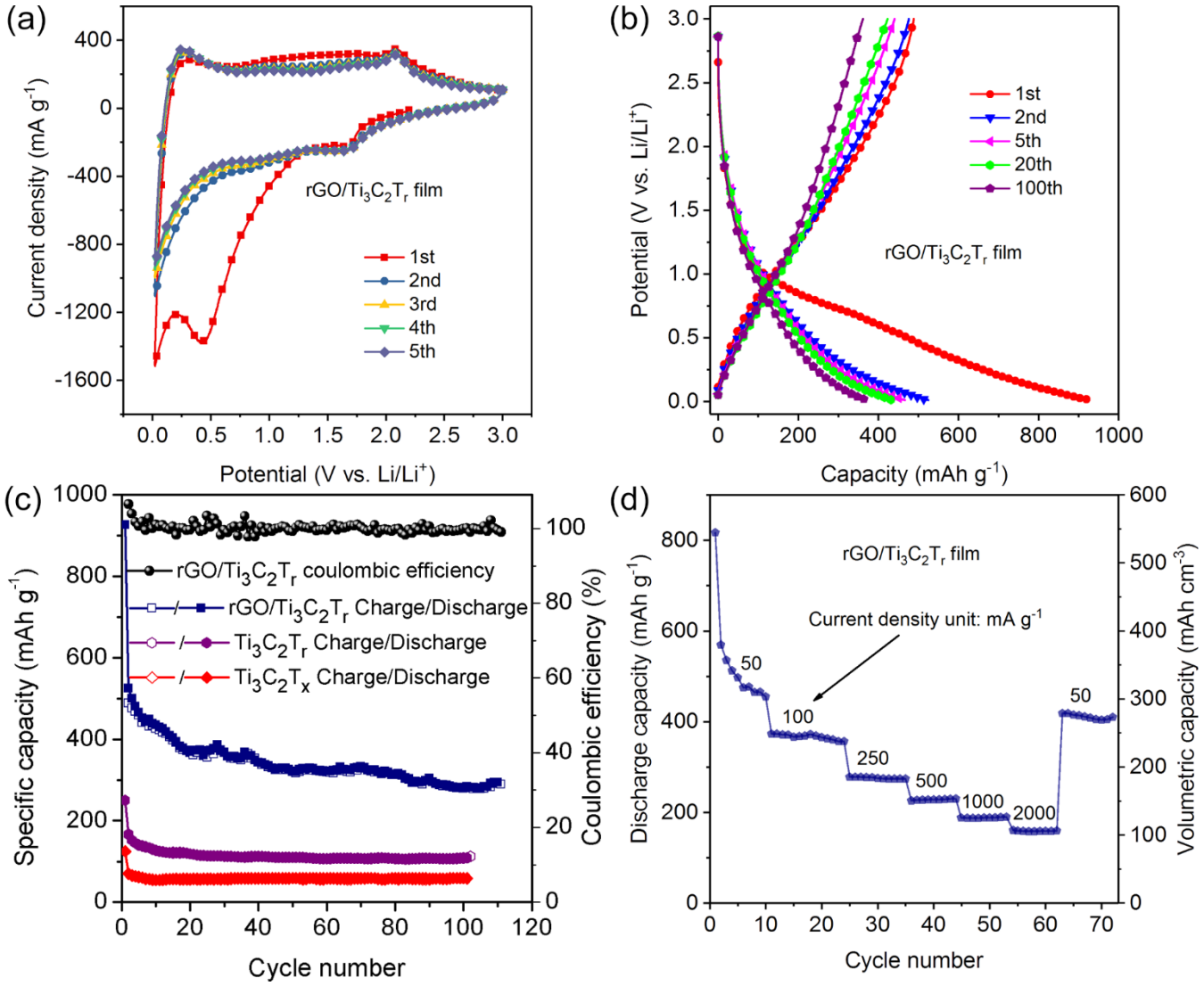

Figure 6. a) CV curves of rGO/$Ti_3C_2T_r$ electrode at a scan rate of 0.5 mV s^{-1}. b) Charge-discharge profiles of rGO/$Ti_3C_2T_r$ electrode at different cycles with a current density of 0.1 A g^{-1}. c) Cycling performance and coulombic efficiency at a current density of 0.1 A g^{-1}. d) Rate performance of hybrid rGO/$Ti_3C_2T_r$ electrode.

Table 1. Comparison of the electrochemical performance of various MXene-based anode materials for Li-ion storage

Sample	Current density (A g^{-1})	Cycle number	Reversible capacity (mAh g^{-1})	Reference
Ti_2CT_x anode material	0.12	80	110	[19]
$Ti_3C_2T_x$ paper	0.4	100	400	[20]
$Ti_3C_2T_x$/rGO films	0.1	100	280	[29]
Ti_2CT_x	0.14	100	140	[18]
$Ti_3C_2T_x$/CNT paper	0.6	100	600	[37]
$Ti_3C_2T_x$ disc	0.03	50	110	[38]
$Ti_3C_2T_x$	0.12	100	124	[39]
rGO/Ti_2CT_r film	0.1	100	700	This work
rGO/$Ti_3C_2T_r$ film	0.1	100	305	This work

This simple and effective method can also be applied for treating other MXenes and fabricating other rGO/MXene films. In this work, rGO/$Ti_3C_2T_r$ films were also fabricated using the similar method. Additionally, the effect of the thermal treatment on the electrochemical performance of $Ti_3C_2T_x$ is evaluated. As shown in Figure S5a, c, owing to the removal of surface group (-OH), the CV curves of $Ti_3C_2T_r$ presented pseudo-rectangular shape without obvious lithiation and delithiation peaks in comparison to $Ti_3C_2T_x$. After removal of the termination groups (-OH) on $Ti_3C_2T_x$, the reversible capacity (at current density of 0.1 A g^{-1}) increased from 55 mAh g^{-1} of $Ti_3C_2T_x$ to 125 mAh g^{-1} of $Ti_3C_2T_r$ (Figure S5b, d and Figure 6c). Furthermore, rGO/$Ti_3C_2T_r$ film was also fabricated and its electrochemical properties were evaluated using Li ion half-cells. Combining $Ti_3C_2T_r$ with rGO nanosheets, the CV profiles of the rGO/$Ti_3C_2T_r$ film (Figure 6a) showed a pseudo-rectangular shape, without obvious lithiation and delithiation peaks, which is similar to the case of rGO/Ti_2CT_r film. The charge/discharge profiles (Figure 6b) were sloping over the potential range of 0.01-3 V vs. Li^+/Li. At current density of 0.1 A g^{-1}, the first-cycle discharge capacity was approximately 930 mAh g^{-1} (Figure 6c). After the first cycle, the capacity gradually decreased with increasing cycle number and remained at 305 mAh g^{-1} after 100 cycles. The first-cycle irreversibility, and initial capacity drop, can be attributed to the formation of a SEI layer and possible irreversible reactions between Li ions and electrode materials. The rGO/$Ti_3C_2T_r$ film electrodes exhibited good specific capacities even at high rates (Figure 6d). At 50 mA g^{-1}, a capacity of 480 mAh g^{-1} was achieved. Capacities of approximately 230 mAh g^{-1} at 500 mA g^{-1} and approximately 160 mAh g^{-1} at 2000 mA g^{-1} were observed. As shown in Table 1, compared with other MXene-based anode materials, thermal reduced porous rGO/MXene films exhibit competitive capacities. Therefore, the results above demonstrate that the rGO/MXene electrodes can be used as promising flexible anodes for Li-ion storage. They can be fabricated by vacuum-assisted filtration, spray coating or other methods, followed by thermal reduction under vacuum or in an inert environment, promoting the applications of MXene-based anode materials in Li-ion batteries and capacitors.

Conclusions

Flexible freestanding rGO/Ti_2CT_r and rGO/$Ti_3C_2T_r$ film electrodes were fabricated by vacuum-assisted filtration followed by thermal reduction. The surface functional groups of MXenes and GO can be removed at the same time during annealing, resulting in an improved contact and electronic transport between MXene and rGO nanosheets. rGO can act as a conductive binder to link the separated layers of MXenes and connect the MXene particles, improving the conductivity of the anode. In turn, the MXene particles impede the agglomeration of rGO nanosheets. It has been demonstrated that flexible freestanding film electrodes with enhanced electrochemical performance for Li-ion storage can be produced by combining MXene with rGO. They exhibit good reversible capacity, improved coulombic efficiency, excellent cycling stability, and rate performance. At current density of 0.1 A g^{-1}, reversible capacities of 700 mAh g^{-1} and 305 mAh g^{-1} were recorded for rGO/Ti_2CT_r and rGO/$Ti_3C_2T_r$, respectively. Furthermore, the terminal -OH groups on MXenes can be removed without phase transformation by thermal treatment at 573K in vacuum, resulting in improved electrical conductivity and electrochemical performance of MXenes (Ti_2CT_x and $Ti_3C_2T_x$) due to the more efficient charge-transfer process. These results will facilitate rapid development and applications of MXene-based electrodes in Li-ion capacitors and batteries.

Experimental Section

Synthesis of Ti_2AlC

Ti_2AlC powder was synthesized by pressureless sintering the mixed powders of titanium (Aladdin Reagent, -325 mesh, 99.8%), aluminum (Aladdin Reagent, -325 mesh, 99.5%), and graphite (Aladdin Reagent, crystalline, -325 mesh, 99%) in a molar ratio of 2:1.1:1 at 1300 ˚C for 40 min. After sintering, the product was milled and sieved through a 400 mesh sieve producing powder with particle size less than 38 μm.

Synthesis and thermal treatment of Ti_2CT_x

Concentrated HCl was diluted with distilled water to produce a 6 M solution (30 ml). 2 g LiF was added to the solution, with stirring for 30 min using a magnetic Teflon stir bar to dissolve the salt. 2 g of Ti_2AlC powder was gradually added to the mixed solution to avoid the violent exothermic reaction. The suspension was held at 40 ˚C for 12 h. After that the mixture was washed about 4 times through repeated procedure of distilled water, centrifugation, and decanting, until the pH of supernatant reaches a pH of approximately 6. The final product was filtered with a small amount of water. Then the wet sediment was dried in a desiccator under vacuum at room temperature to obtain Ti_2CT_x MXene powder. The as-prepared Ti_2CT_x was then calcined at 300 ˚C (573K) in vacuum for 5h, and renamed as Ti_2CT_r. A similar procedure was used to prepare $Ti_3C_2T_r$. The experimental details of synthesis of $Ti_3C_2T_x$ can be seen in the supporting information.

Preparation of porous rGO/Ti_2CT_r and rGO/$Ti_3C_2T_r$ films

Graphite oxide was prepared using a modified Hummer's method.[40] The GO colloidal suspension (1 mg mL^{-1}) was obtained by exfoliating graphite oxide via sonication for 1 h. The hydrophilic Ti_2CT_x was dispersed in water by sonication, producing a stable Ti_2CT_x-water dispersion (1 mg mL^{-1}). The GO-water and

Ti_2CT_x-water dispersions were mixed to obtain a GO/Ti_2CT_x hybrid colloidal suspension with GO/Ti_2CT_x mass ratio of 3:1. Then the hybrid suspension was vacuum-filtered through a cellulose filter (diameter: 5 cm; pore size: 0.22 μm), followed by drying in air. The obtained GO/Ti_2CT_x films could be easily peeled off from the cellulose filter. Afterwards, the GO/Ti_2CT_x samples were thermally treated at 573K for 5 h under vacuum to obtain freestanding rGO/Ti_2CT_r films. During the thermal reduction process, the dielectric oxygen-containing functional groups on the surface of Ti_2CT_x and GO can be removed at the same time, resulting in improved conductivity between Ti_2CT_r and rGO nanosheets. The rGO/$Ti_3C_2T_r$ films were fabricated by a similar method.

Electrode preparation and electrochemical tests in lithium half-cells

rGO/MXene films (rGO/Ti_2CT_r and rGO/$Ti_3C_2T_r$) themselves can be directly used as working electrodes in the electrochemical tests without using metal current collectors. The working electrodes of Ti_2CT_x, Ti_2CT_r, $Ti_3C_2T_x$ and $Ti_3C_2T_r$ powders were prepared by mixing active materials with carbon black, and polyvinylidene fluoride (PVDF) binder in N-methyl-2-pyrrolidinone (NMP) with a weight ratio of 8:1:1 and the resulting slurries were pasted on a copper foil and then dried at 90 °C in vacuum. Li-ion half-cells were assembled as coin cells (CR2032 type) with lithium foils as the counter electrodes and polypropylene membranes (3501 Coated PP, Celgard) as separators. The cell assembly was conducted in an argon-filled glove box. The electrolyte was 1 M $LiPF_6$ in a 1:1 mixture of ethylene carbonate (EC) and dimethyl carbonate (DMC). The galvanostatic charge-discharge tests were performed on a LAND battery tester system between 0.01 and 3.0 V at room temperature. Cyclic voltammetry (CV) measurements at a scan rate of 0.5 mV s^{-1} within 0-3 V and electrochemical impedance spectroscopy (EIS) measurements with the frequency ranging from 100 kHz to 10 mHz were conducted with a CHI660D electrochemical workstation. Gravimetric capacities were calculated from the total mass of composite electrodes.

Characterization of materials

X-ray diffraction (XRD) patterns were recorded with step-scanning powder diffractometer (Smartlab, Rigaku, Japan) using Cu-Kα radiation with a step size of 0.02˚ and dwelling time of 0.2 s. The microstructures of the materials were observed by scanning electron microscopy (SEM, MEGALLAN 400) and transmission electron microscopy (TEM, JEOL JEM-2100, Japan), using an accelerating voltage of 200 kV. Surface functional groups were examined by Fourier transform infrared spectroscopy (FTIR, Bruker Optiks E55+FRA106, Germany). Thermogravimetric analysis and differential scanning calorimetry analysis (TG-DSC) of MXene were performed using a Setaram Evolution 2400 thermal analyzer with α-Al_2O_3 pans under argon flow of 20 mL min^{-1} with a heating rate of 15 ˚C min^{-1} from room temperature to 700 ˚C. Chemical compositions and oxidation state of the samples were further analyzed using high resolution X-ray photoelectron spectroscopy (XPS) with monochromated Al Kα radiation (hv = 1486.6 eV). Binding energies were referenced to that of free carbon at 284.8 eV. The peak fitting was carried out using commercially available software, CasaXPS. Brunauer-Emmett-Teller (BET)-specific surface area were conducted using nitrogen adsorption on a gas sorption analyzer (JW-BK132F). The pore size distributions were calculated by the Barrett–Joyner–Halenda (BJH) method, and the BJH analysis was done from the desorption branch of the isotherms.

Acknowledgements

The authors sincerely acknowledge financial support from the General Programs of the National Natural Science Foundation of China (21571080), the national long-term project (WQ20152200273) of “Thousand Talents Plan of Bureau of Foreign Experts Affairs” of People’s Republic of China, and the Natural Science Foundation of Jilin province (20170101193JC).

Keywords: MXene • graphene • porous film • flexible anode • Li-ion storage

[1] M. R. Lukatskaya, B. Dunn, Y. Gogotsi, *Nat. Commun.* **2016**, *7,* 126477.

[2] D. P. Dubal, O. Ayyad, V. Ruiz, P. Gomez-Romero, *Chem. Soc. Rev.* **2015**, *44,* 1777-1790.

[3] Y. Gogotsi, *ACS Nano* **2014**, *8,* 5369-5371.

[4] M. Q. Zhao, M. Torelli, C. E. Ren, M. Ghidiu, Z. Ling, B. Anasori, M. W. Barsoum, Y. Gogotsi, *Nano Energy* **2016**, *30,* 603-613.

[5] W. S. Chang, C. M. Park, J. H. Kim, Y. U. Kim, G. Jeongc, H. J. Sohn, *Energy Environ. Sci.* **2012**, *5,* 6895.

[6] L. L. Wang, D. Chen, K. Jiang, G. Z. Shen, *Chem. Soc. Rev.* **2017**, 46*,* 6764-6815.

[7] J. Y. Liu, X. X. Li, J. R. Huang, J. J. Li, P. Zhou, J. H. Liuad, X. J. Huang, *J. Mater. Chem. A* **2017**, *5,* 5977-5994.

[8] J. Xiao, D. Choi, L. Cosimbescu, P. Koech, J. Liu, J. P. Lemmon, *Chem. Mater.* **2010**, *22,* 4522-4524.

[9] Z. Deng, H. Jiang, Y. Hu, Y. Liu, L. Zhang, H. Liu, C. Li, *Adv. Mater.* **2017**, *29,* 1603020.

[10] H. Huang, S. Gao, A. M. Wu, K. Cheng, X. N. Li, X. X. Gao, J. J. Zhao, X. L. Dong, G. Z. Cao, *Nano Energy* **2017**, *31,* 74-83.

[11] P. Wang, R. Wang, J. Lang, X. Zhang, Z. Chen, X. Yan, *J. Mater. Chem. A* **2016**, *4,* 9760-9766.

[12] M. Li, F. Pan, E. S. G. Choo, Y. Lv, Y. Chen, J. Xue, *ACS Appl. Mater. Interfaces* **2016**, *8,* 6972-6981.

[13] J. Liang, Y. Zhao, L. Guo, L. Li, *ACS Appl. Mater. Interfaces* **2012**, *4,* 5742-5748.

[14] S. Sun, C. Liao, A. M. Hafez, H. Zhu, S. Wu, *Chem. Eng. J.* **2018**, *338,* 27-45.

[15] B. Anasori, M. R. Lukatskaya, Y. Gogotsi, *Nat. Rev. Mater.* **2017**, *2,* 16098.

[16] M. Naguib, O. Mashtalir, J. Carle, V. Presser, J. Lu, L. Hultman, Y. Gogotsi, M. W. Barsoum, *ACS Nano* **2012**, *6,* 1322-1331.

[17] J. Luo, X. Tao, J. Zhang, Y. Xia, H. Huang, L. Zhang, Y. Gan, C. Liang, W. Zhang, *ACS Nano* **2016**, *10,* 2491-2499.

[18] J. Come, M. Naguib, P. Rozier, M. W. Barsoum, Y. Gogotsi, P. L. Taberna, M. Morcrette, P. Simon, *J. Electrochem. Soc.* **2012** *159,* A1368-A1373.

[19] M. Naguib, J. Come, B. Dyatkin, V. Presser, P. L. Taberna, P. Simon, M. W. Barsoum, Y. Gogotsi, *Electrochem. Commun.* **2012**, *16,* 61-64.

[20] O. Mashtalir, M. Naguib, V. N. Mochalin, Y. Dall'Agnese, M. Heon, M. W. Barsoum, Y. Gogotsi, *Nat. Commun.* **2013**, *4,* 1716.

[21] A. Byeon, A. M. Glushenkov, B. Anasori, P. Urbankowski, J. Li, B. W. Byles, B. Blake, K. L. Van Aken, S. Kota, E. Pomerantseva, J. W. Lee, Y. Chen,

Y. Gogotsi, *J. Power Sources* **2016**, *326,* 686-694.

[22] X. Xie, M. Q. Zhao, B. Anasori, K. Maleski, C. E. Ren, J. Li, B. W. Byles, E. Pomerantseva, G. Wang, Y. Gogotsi, *Nano Energy* **2016**, *26,* 513-523.

[23] J. Luo, W. Zhang, H. Yuan, C. Jin, L. Zhang, H. Huang, C. Liang, Y. Xia, J. Zhang, Y. Gan, X. Tao, *ACS Nano* **2017**, *11,* 2459-2469.

[24] M. Khazaei, A. Ranjbar, M. Arai, T. Sasaki, S. Yunoki, *J. Mater. Chem. C* **2017**, *5,* 2488-2503.

[25] Y. Dall'Agnese, M. R. Lukatskaya, K. M. Cook, P. L. Taberna, Y. Gogotsi, P. Simon, *Electrochem. Commun.* **2014**, *48,* 118-122.

[26] J. Li, X. Yuan, C. Lin, Y. Yang, L. Xu, X. Du, J. Xie, J. Lin, J. Sun, *Adv. Energy Mater.* **2017**, *7,* 1602725.

[27] W. Lv, D. M. Tang, Y. B. He, C. H. You, Z. Q. Shi, X. C. Chen, C. M. Chen, P. X. Hou, C. Liu, Q. H. Yang, *ACS nano* **2009**, *3,* 3730-3736.

[28] J. Yan, C. E. Ren, K. Maleski, C. B. Hatter, B. Anasori, P. Urbankowski, A. Sarycheva, Y. Gogotsi, *Adv. Funct. Mater.* **2017**, *27,* 1701264.

[29] Z. Ma, X. Zhou, W. Deng, D. Lei, Z. Liu, *ACS Appl. Mater. Interfaces* **2018**, *10,* 3634-3643.

[30] E. Pomerantseva, Y. Gogotsi, *Nature Energy* **2017**, *2,* 17089.

[31] M. Ghidiu, M. R. Lukatskaya, M. Q. Zhao, Y. Gogotsi, M. W. Barsoum, *Nature* **2014**, *516,* 78-81.

[32] Q. Peng, J. Guo, Q. Zhang, J. Xiang, B. Liu, A. Zhou, R. Liu, Y. Tian, *J. Am. Chem. Soc.* **2014**, *136,* 4113-4116.

[33] J. Li, Y. Du, C. Huo, S. Wang, C. Cui, *Ceram. Int.* **2015**, *41,* 2631-2635.

[34] Z. Li, L. Wang, D. Sun, Y. Zhang, B. Liu, Q. Hu, A. Zhou, *Mat. Sci. Eng. B* **2015**, *191,* 33-40.

[35] M. Naguib, J. Halim, J. Lu, K. M. Cook, L. Hultman, Y. Gogotsi, M. W. Barsoum, *J. Am. Chem. Soc.* **2013**, *135,* 15966-15969.

[36] X. Liu, D. Chao, Y. Li, J. Hao, X. Liu, J. Zhao, J. Lin, H. Fan, Z. Shen, *Nano Energy* **2015**, *17,* 43-51.

[37] C. E. Ren, M. Q. Zhao, T. Makaryan, J. Halim, M. Boota, S. Kota, B. Anasori, M. W. Barsoum, Y. Gogotsi, *ChemElectroChem* **2016**, *3,* 689-693.

[38] S. J. Kim, M. Naguib, M. Zhao, C. Zhang, H. T. Jung, M. W. Barsoum, Y. Gogotsi, *Electrochim. Acta* **2015**, *163,* 246-251.

[39] D. Sun, M. Wang, Z. Li, G. Fan, L. Z. Fan, A. Zhou, *Electrochem. Commun.* **2014**, *47,* 80-83.

[40] W. S. Hummers Jr., R. E. Offema, *J. Am. Chem. Soc.* **1958**, *80,* 1339.

Entry for the Table of Contents

FULL PAPER

Flexible freestanding hybrid rGO/MXene films with enhanced Li-ion storage capacity are fabricated by vacuum-assisted filtration method followed by a simple thermal treatment. In the hybrid films reduced graphene oxide nanosheets act as a binder, which bridges electrochemically active conducting MXene particles. The effect of the surface functional group (-OH) on Li-storage performance of MXenes is evaluated.

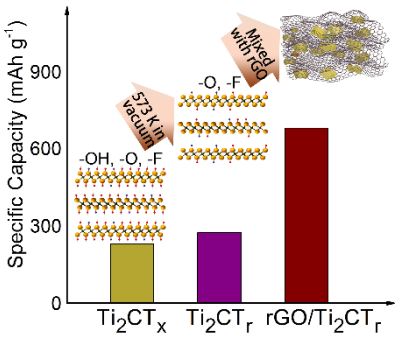

Shuaikai Xu,[a] Yohan Dall'Agnese,[a] Junzhi Li,[a] Yury Gogotsi,[a, b] and Wei Han*[a, c]*

Thermally reduced graphene/MXene film for enhanced Li-ion storage